

Imbalance-Robust and Sampling-Efficient Continuous Conditional GANs via Adaptive Vicinity and Auxiliary Regularization

Xin Ding^{1,2*}, Yun Chen^{1,2}, Yongwei Wang³, Kao Zhang^{1,2}, Sen Zhang¹, Peibei Cao^{1,2}, Xiangxue Wang¹,

¹ School of Artificial Intelligence/School of Future Technology, Nanjing University of Information Science & Technology

² Perceptual and Generative AI Lab, Nanjing University of Information Science & Technology

³ College of Media, Zhejiang University

{dingxin, 202412491483, kaozhang, senzhang, 003970, xwang}@nuist.edu.cn, yongwei.wang@zju.edu.cn

Abstract

Recent advances in conditional generative modeling have introduced Continuous conditional Generative Adversarial Network (CcGAN) and Continuous Conditional Diffusion Model (CCDM) for estimating high-dimensional data distributions conditioned on scalar, continuous regression labels (e.g., angles, ages, or temperatures). However, these approaches face fundamental limitations: CcGAN suffers from data imbalance due to fixed-size vicinity constraints, while CCDM requires computationally expensive iterative sampling. We present CcGAN-AVAR, an enhanced CcGAN framework that addresses both challenges: (1) leveraging the GAN framework’s native one-step generation to overcome CCDMs’ sampling bottleneck (achieving 300x-2000x faster inference), while (2) two novel components specifically target data imbalance - an adaptive vicinity mechanism that dynamically adjusts vicinity’s size, and a multi-task discriminator that constructs two regularization terms (through auxiliary regression and density ratio estimation) to significantly improve generator training. Extensive experiments on four benchmark datasets (64x64 to 192x192 resolution) across eight challenging imbalanced settings demonstrate that CcGAN-AVAR achieves state-of-the-art generation quality while maintaining sampling efficiency.

Code — <https://github.com/UBCDingXin/CcGAN-AVAR>

1 Introduction

Continuous Conditional Generative Modeling (CCGM), illustrated in Figure 1, learns high-dimensional data distributions (typically images) conditioned on continuous scalar regression labels (e.g., angles and ages). This capability has proven valuable across diverse applications including engineering inverse design (Heyrani Nobari, Chen, and Ahmed 2021; Zhao et al. 2024; Fang, Shen, and Wang 2023), hyperspectral image synthesis (Zhu et al. 2023), controllable point cloud generation (Triess et al. 2022), CO₂ propagation prediction (Ferreira et al. 2022), and integrated circuit design (Park et al. 2022). However, CCGM faces unique challenges: the inherent scarcity (or complete absence) of training samples for specific label values fundamentally limits the effectiveness of conventional *conditional Generative Adversarial Networks* (cGANs) (Kang et al. 2023) and *Conditional Diffusion Models* (CDMs) (Peebles and Xie 2023).

*Corresponding author.

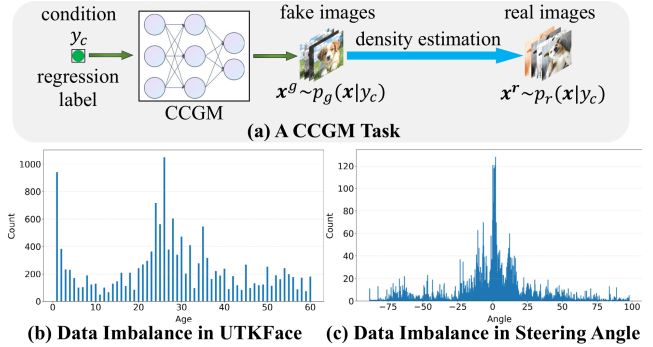


Figure 1: The illustration of CCGM with data imbalance in UTKFace and Steering Angle datasets.

To mitigate data scarcity, Ding et al. (2021, 2023b) proposed the *Continuous conditional Generative Adversarial Network* (CcGAN), which estimates the target data distribution $p_r(\mathbf{x}|y_c)$ by incorporating training samples within a fixed-size hard or soft vicinity of the conditional label y_c . While these vicinities enable CcGAN to trade some label consistency—the degree to which generated samples align with the given condition—for improved training stability and generation quality, Figure 2(a)–(b) reveals a critical limitation: the fixed-size vicinities may unnecessarily compromise too much label consistency for densely sampled label values, ultimately leading to suboptimal generation performance.

As an alternative to CcGAN, Ding et al. (2025) recently integrated CcGAN techniques into diffusion models, proposing the *Continuous Conditional Diffusion Model* (CCDM). Although CCDM exhibits superior generation quality and robustness to data imbalance compared to CcGAN, its sampling process is 700–2000x slower, severely limiting practical deployment. While distillation-based one-step sampling mitigates this latency, it incurs significant generation quality degradation and additional training overhead (Ding et al. 2025). Thus, achieving both high-quality generation and efficient sampling remains an open challenge in CCGM.

Motivated by these limitations, we present CcGAN-AVAR, an improved CcGAN framework that achieves generation quality comparable to or surpassing CCDM while maintaining significantly faster sampling speeds (300x-2000x accel-

eration). Our key contributions include: (1) a novel soft/hybrid Adaptive Vicinity (AV) mechanism that overcomes the limitations of conventional hard/soft vicinities in handling data imbalance; (2) a multi-task discriminator with dedicated auxiliary branches for noise-insensitive regression and density ratio estimation, generating two auxiliary regularization terms that substantially improve generation quality and label consistency; (3) RC-49-I, an imbalanced variant of the RC-49 dataset (Ding et al. 2023b) incorporating three distinct imbalance patterns (unimodal, bimodal, and trimodal distributions) for thorough evaluation of CCGM methods under realistic data scarcity conditions; and (4) an optimized, unified codebase for CcGAN supporting multiple benchmark datasets, flexible network architecture and vicinity selection, various loss functions, exponential moving average, and mixed-precision training.

2 Related Work

2.1 Continuous Conditional Generative Models

To address data scarcity in CCGM tasks, CcGAN (Ding et al. 2021, 2023b) leverages samples within a label-dependent vicinity of y_c to approximate the data distribution $p_r(\mathbf{x}|y_c)$. The framework introduces two distinct vicinity formulations (hard vicinity and soft vicinity), which leads to the *Hard/Soft Vicinal Discriminator Loss* (HVDL/SVDL) and the corresponding generator loss for CcGAN:

$$\begin{aligned} \mathcal{L}(D) &= \\ & - \frac{1}{N^r} \sum_{j=1}^{N^r} \sum_{i=1}^{N^r} \mathbb{E}_{\epsilon \sim \mathcal{N}(0, \sigma^2)} [W_i^r \log(D(\mathbf{x}_i^r, y_j^r + \epsilon))] \\ & - \frac{1}{N^g} \sum_{j=1}^{N^g} \sum_{i=1}^{N^g} \mathbb{E}_{\epsilon \sim \mathcal{N}(0, \sigma^2)} [W_i^g \log(1 - D(\mathbf{x}_i^g, y_j^g + \epsilon))], \quad (1) \\ \mathcal{L}(G) &= \\ & - \frac{1}{N^g} \sum_{i=1}^{N^g} \mathbb{E}_{\epsilon \sim \mathcal{N}(0, \sigma^2)} \log(D(G(\mathbf{z}_i, y_i^g + \epsilon), y_i^g + \epsilon)), \quad (2) \end{aligned}$$

where D and G denote the discriminator and generator networks, superscripts r/g indicate real/fake samples, \mathbf{z}_i represents Gaussian noise, σ is a positive hyperparameter, and N^r/N^g denote real/fake sample sizes. As illustrated in Figure 2(a), the hard vicinity defines a closed interval centered at y_c with a fixed radius κ . Thus, the weights W_i^r and W_i^g for HVDL are defined as follows:

$$W_i^r = \frac{\mathbb{1}_{\{|y_j^r + \epsilon - y_i^r| \leq \kappa\}}}{N_{y_j^r + \epsilon, \kappa}^r}, \quad W_i^g = \frac{\mathbb{1}_{\{|y_j^g + \epsilon - y_i^g| \leq \kappa\}}}{N_{y_j^g + \epsilon, \kappa}^g}, \quad (3)$$

with $\mathbb{1}_{\{\cdot\}}$ as the indicator function and $N_{y_c, \kappa}$ counting samples in the hard vicinity $[y_c - \kappa, y_c + \kappa]$. Ding et al. (2023b) provides a rule of thumb to compute κ and σ from samples. For soft vicinity, all samples are used to estimate $p_r(\mathbf{x}|y_c)$, but each sample \mathbf{x}_i is assigned with a weight W_i , with the following formulation:

$$W_i^r = \frac{w(y_i^r, y_j^r + \epsilon)}{\sum_{i=1}^{N^r} w(y_i^r, y_j^r + \epsilon)}, \quad W_i^g = \frac{w(y_i^g, y_j^g + \epsilon)}{\sum_{i=1}^{N^g} w(y_i^g, y_j^g + \epsilon)}. \quad (4)$$

As illustrated in Figure 2(b), the soft vicinity weights in Eq. (4) follow an exponential decay curve $w(y, y') =$

$e^{-\nu(y-y')^2}$, where the decay rate $\nu > 0$ controls the weighting sensitivity to label distances. Ding et al. (2023b) set $\nu = 1/\kappa^2$ and exclude samples with soft weights below 10^{-3} from discriminator updates for computational efficiency.

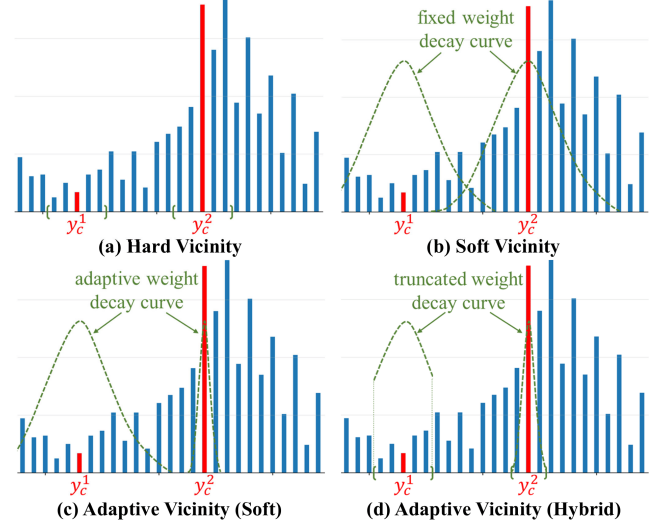


Figure 2: Comparison of traditional fixed-size (hard/soft) vicinities versus our proposed (soft/hybrid) adaptive vicinities. Bar heights represent sample sizes per label value, with y_c^1 and y_c^2 marking two conditional label values exhibiting different local sample densities.

The conventional hard/soft vicinity (with constant κ and ν) often produces suboptimal generation quality on imbalanced datasets. As Figure 2(a)-(b) shows, while samples cluster densely around y_c^2 , the fixed-size vicinity formulation either incorporates excessive samples (hard vicinity) or over-weights distant samples (soft vicinity), both of which significantly degrade label consistency.

Recent work by Ding et al. (2025) introduces CCDM, which incorporates vicinal techniques into diffusion models as a replacement for CcGAN. Although both their empirical study and the experiments in this paper (Tables 1 and 2) show CCDM outperforms conventional CcGANs while maintaining data imbalance robustness, its prohibitively slow sampling speed significantly limits practical applicability.

2.2 Sample-Based Density Ratio Estimation

Ding et al. (2023a) introduced cDR-RS, a sample-based *Density Ratio Estimation* (DRE) method for conditional GANs that computes $r(\mathbf{x}|y) = p_r(\mathbf{x}|y)/p_g(\mathbf{x}|y)$. The estimated density ratios enable rejection sampling to enhance output quality in both class-conditional GANs and CcGANs.

cDR-RS's DRE framework employs a two-stage architecture: a fixed, pre-trained encoder that maps input images \mathbf{x} into latent representations \mathbf{h} , and a trainable 5-layer fully-connected network f_{dre} that processes \mathbf{h} for density ratio estimation. During optimization, only f_{dre} is updated using the following penalized Softplus loss:

$$\mathcal{L}(f_{\text{dre}}) = \frac{1}{N^g} \sum_{i=1}^{N^g} [\delta(f_{\text{dre}}(\mathbf{h}_i^g|y_i^g)) f_{\text{dre}}(\mathbf{h}_i^g|y_i^g) - \eta(f_{\text{dre}}(\mathbf{h}_i^g|y_i^g))]$$

$$-\frac{1}{N^r} \sum_{i=1}^{N_r} \delta(f_{\text{dre}}(\mathbf{h}_i^r | y_i^r)) + \lambda_{\text{dre}} \cdot \left(\frac{1}{N^g} \sum_{i=1}^{N^g} f_{\text{dre}}(\mathbf{h}_i^g | y_i^g) - 1 \right)^2, \quad (5)$$

where δ and η denote respectively the Sigmoid and Softplus functions, and λ_{dre} is a hyperparameter for regularization.

3 Method

3.1 Overview

In this section, we present CcGAN-AVAR, an improved CcGAN framework designed to address data imbalance challenges. As illustrated in Figure 3, our approach introduces two key innovations: (1) a novel soft/hybrid adaptive vicinity mechanism that dynamically adjusts to local sample density, and (2) a multi-task discriminator that generates two auxiliary regularization terms to enhance generator training.

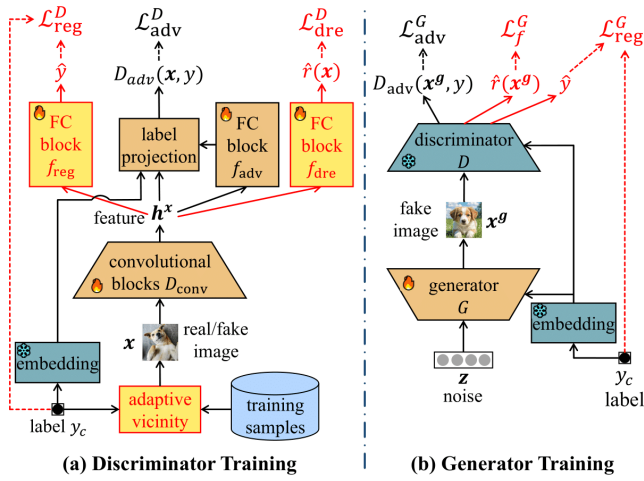


Figure 3: Overall workflow of CcGAN-AVAR

3.2 Adaptive Vicinity for Imbalanced Data

Let $Q^r = \{(\mathbf{x}_i^r, y_i^r)\}_{i=1}^{N^r}$ denote a training set of N^r real image-label pairs, where the labels consist of M distinct values $Y^u = \{y_{(1)}, \dots, y_{(M)}\}$ sorted in strictly increasing order ($y_{(i)} < y_{(i+1)}$ for $i = 1, \dots, M$). For i -th distinct label value $y_{(i)}$, we denote by N_i its corresponding sample count. In severely imbalanced datasets, N_i exhibits substantial variation across different i , as demonstrated in Figure 1(b)-(c).

To address data imbalance, we propose two distinct types of *Adaptive Vicinity* (AV): Soft AV and Hybrid AV. Both approaches replace the vicinity parameters κ and ν in Eqs. (3) and (4) with a new hyperparameter N_{AV} , which determines the *minimum number of effective samples per vicinity*. Practical guidance for setting N_{AV} is provided in the Appendix.

(1) Soft Adaptive Vicinity

Building on CcGAN’s empirically demonstrated superiority of soft vicinity over hard vicinity (Ding et al. 2021, 2023b), we first propose a soft AV mechanism (Figure 2(c)). During discriminator training, we create a target conditional label y_c by randomly adding Gaussian noise to a training

label (e.g., $y_j^r + \epsilon$ in Eq. (1)). Without loss of generality, assuming y_c lies between $y_{(i-1)}$ and $y_{(i)}$, we initialize a hard vicinity centered at y_c with zero-radius boundaries ($\kappa_l = 0, \kappa_r = 0$) containing $N_c = 0$ samples. This vicinity then extends iteratively until $N_c \geq N_{\text{AV}}$: at each step, the vicinity extends leftwards if the leftmost external label is closer to y_c than the rightmost external label, and rightwards otherwise. Following each extension, we update either κ_l or κ_r to reflect the distance of the newly incorporated label to y_c , while incrementing N_c by the sample count at this label. Upon reaching $N_c \geq N_{\text{AV}}$, we obtain the final radius $\kappa_{y_c} = \max(\kappa_l, \kappa_r)$, which determines the local weight decay rate $\nu_{y_c} = 1/\kappa_{y_c}^2$. Soft weights are then assigned to all training samples via Eq. (4) using ν_{y_c} , with Figure 4 illustrating this process.

This adaptive approach automatically adjusts to local sample density: in dense regions (small κ_{y_c}), weights decay rapidly to maintain label consistency while preserving diversity; in sparse regions (large κ_{y_c}), weights decay slowly to incorporate more distant samples, ensuring training stability and preventing mode collapse.

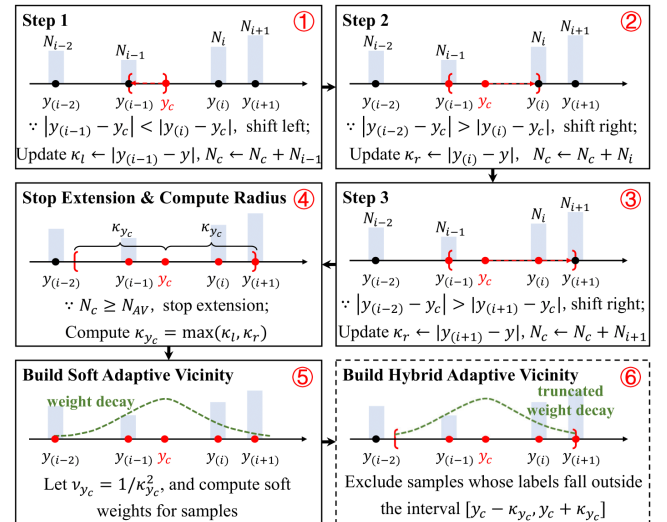


Figure 4: Illustrative example: Building the soft or hybrid adaptive vicinity for condition y_c through 3 extension steps

(2) Hybrid Adaptive Vicinity

We further propose a hybrid AV mechanism (Figs. 2(d) and 4) that extends the soft AV approach. This hybrid variant incorporates truncated weight decay by assigning zero weights to samples outside the interval $[y_c - \kappa_{y_c}, y_c + \kappa_{y_c}]$. By combining the adaptive weighting of soft AV with the boundary constraints of hard vicinity, this approach can further enhance label consistency.

3.3 Auxiliary Generator Regularization

(1) A Multi-Task Discriminator

We propose a multi-task discriminator framework $D(\mathbf{x}, y)$, with architecture illustrated in Figure 3 (a). In our implementation, the backbone of D consists of the convolutional blocks from SNGAN (Miyato et al. 2018), denoted as D_{conv} , though this component can be readily replaced with alternative GAN

architectures such as DCGAN (Radford, Metz, and Chintala 2015), SAGAN (Zhang et al. 2019), BigGAN (Brock, Donahue, and Simonyan 2019), or GigaGAN (Kang et al. 2023). The convolutional backbone is followed by three parallel fully-connected branches: an one-layer adversarial branch f_{adv} , a two-layer regression branch f_{reg} , and a three-layer density ratio estimation branch f_{dre} .

The adversarial output, denoted by $D_{\text{adv}}(\mathbf{x}, y)$, is generated by processing the extracted features $\mathbf{h}^{\mathbf{x}} = D_{\text{conv}}(\mathbf{x}, y)$ through the adversarial branch f_{adv} combined with label projection (Miyato et al. 2018). This output is then used to compute the adversarial loss $\mathcal{L}_{\text{adv}}^D$ according to Eqs. (1) and (4). Notably, the proposed soft or hybrid AV mechanism is fully compatible with this computation.

The regression branch f_{reg} predicts the label of the input image through $\hat{y} = f_{\text{reg}}(D_{\text{conv}}(\mathbf{x}, y))$. To optimize this branch, we employ a γ -insensitive hinge loss adapted from support vector regression (Murphy 2022), formulated as:

$$\mathcal{L}_{\text{reg}}^D = \frac{1}{N^r} \sum_{i=1}^{N^r} \mathbb{E}_{\epsilon \sim \mathcal{N}(0, \sigma^2)} [\max(|y_i^r + \epsilon - \hat{y}_i^r| - \gamma, 0)] + \frac{1}{N^g} \sum_{i=1}^{N^g} \max(|y_i^g - \hat{y}_i^g| - \gamma, 0), \quad (6)$$

where y_i^r and y_i^g denote the ground truth label for \mathbf{x}_i^r and the conditional label used to generate \mathbf{x}_i^g , respectively, while \hat{y}_i^r and \hat{y}_i^g represent the corresponding prediction from f_{reg} . The elasticity parameter $\gamma \geq 0$, empirically set as the maximum radius $\kappa_{y_i^r + \epsilon}$ in a training batch, accounts for Gaussian noise ϵ in real labels and helps mitigate misalignment between \mathbf{x}_i^g and its conditional label y_i^g . In practice, we often replace y_i^g with \tilde{y}_i^g , where \tilde{y}_i^g denotes the output of a ResNet-18 (He et al. 2016) separately trained for label regression on \mathbf{x}_i^g .

The DRE branch f_{dre} predicts the conditional density ratio $r(\mathbf{x}|y) = p_r(\mathbf{x}|y)/p_g(\mathbf{x}|y)$ for real and fake images. This branch is optimized through the loss function $\mathcal{L}_{\text{dre}}^D$ (Eq. (5)), where $\lambda_{\text{dre}} = 10^{-2}$. Unlike Ding et al. (2023a), our feature extractor D_{conv} is jointly optimized with f_{dre} .

The complete discriminator loss function is defined as:

$$\mathcal{L}^D = \mathcal{L}_{\text{adv}}^D + \lambda_{\text{reg}}^D \cdot \mathcal{L}_{\text{reg}}^D + \lambda_{\text{dre}}^D \cdot \mathcal{L}_{\text{dre}}^D, \quad (7)$$

where $\lambda_{\text{reg}}^D \geq 0$ and $\lambda_{\text{dre}}^D \geq 0$ are the weighting coefficients.

(2) Auxiliary Regularization for Generator Training

The generator’s adversarial loss $\mathcal{L}_{\text{adv}}^G$ (Eq. (2)) is supplemented by two additional regularization terms derived from the multi-task discriminator: a regression penalty and a f -divergence penalty. The regression penalty utilizes mean absolute error to quantify label consistency:

$$\mathcal{L}_{\text{reg}}^G = \frac{1}{N^g} \sum_{i=1}^{N^g} |y_i^g - \hat{y}_i^g|. \quad (8)$$

This formulation directly minimizes the discrepancy between \mathbf{x}_i^g and \hat{y}_i^g , thereby enforcing stronger label alignment during image synthesis. The f -divergence penalty, implemented through Pearson χ^2 divergence with $f = (t - 1)^2$ (Nowozin, Cseke, and Tomioka 2016), provides distributional matching:

$$\mathcal{L}_f^G = \frac{1}{N^g} \sum_{i=1}^{N^g} (f_{\text{dre}}(D_{\text{conv}}(\mathbf{x}_i^g, y_i^g)) - 1)^2. \quad (9)$$

This term estimates the f -divergence between $p_r(\mathbf{x}|y)$ and $p_g(\mathbf{x}|y)$, guiding the generator towards more realistic data synthesis. The complete generator loss function combines these components through weighted summation:

$$\mathcal{L}^G = \mathcal{L}_{\text{adv}}^G + \lambda_{\text{reg}}^G \cdot \mathcal{L}_{\text{reg}}^G + \lambda_f^G \cdot \mathcal{L}_f^G, \quad (10)$$

where $\lambda_{\text{reg}}^G \geq 0$ and $\lambda_f^G \geq 0$ are the weighting coefficients.

4 Experiments

4.1 Experimental Setup

Datasets. Building upon established experimental protocols (Ding et al. 2023b; Ding, Wang, and Xu 2024; Ding et al. 2025), we conduct comprehensive evaluations across multiple benchmark datasets: RC-49 (Ding et al. 2023b) (44,051 chair images at 64×64 resolution with rotation angles from 0.1° to 89.9° in 0.1° increments), UTKFace (Zhang, Song, and Qi 2017) (14,723 facial images across 64×64 , 128×128 , and 192×192 resolutions with age labels from 1 to 60), and Steering Angle (Chen 2018) (12,271 driving images at 64×64 and 128×128 resolutions covering steering angles from -80° to 80°). For UTKFace and Steering Angle experiments, all available samples are used for both training and evaluation. The RC-49 experiments employ a curated balanced subset of 11,250 images (25 samples each for 450 distinct angle labels) for training while utilizing the complete collection of 44,051 images for comprehensive evaluation.

To rigorously evaluate model robustness to data imbalance, we introduce RC-49-I—a specialized variant of RC-49 comprising three subsets with distinct label distribution patterns (unimodal, bimodal, and trimodal; see Figure 5). This framework enables systematic comparison between three challenging imbalanced scenarios (UTKFace, Steering Angle, and RC-49-I) and the balanced RC-49 baseline. All models trained on RC-49-I are evaluated using the complete RC-49 dataset (44,051 samples) to ensure consistent assessment.

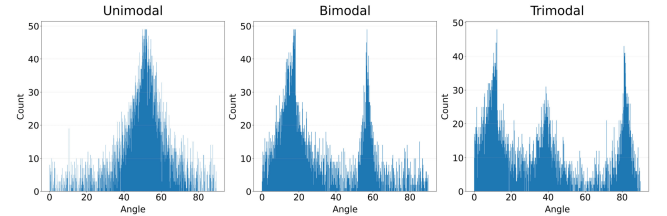


Figure 5: Three data imbalance patterns in RC-49-I

Compared Methods. Our comparative evaluation examines six continuous conditional generative models: CcDPM (Zhao et al. 2024) and CCDM (Ding et al. 2025) as diffusion-based approaches; CcGAN (Ding et al. 2023b) and Dual-NDA (Ding, Wang, and Xu 2024) representing vanilla CcGAN architectures; along with our proposed variants CcGAN-AVAR-S (soft adaptive vicinity) and CcGAN-AVAR-H (hybrid adaptive vicinity).

Implementation Setup. We utilize the released results of CcDPM, CCDM, CcGAN, and Dual-NDA on RC-49, UTKFace, and Steering Angle from (Ding et al. 2025). For our

newly introduced RC-49-I dataset, we implement these baseline methods while maintaining identical experimental configurations to those used for RC-49. As a key contribution of this work, we develop and release an optimized, unified codebase for CcGAN and our proposed CcGAN-AVAR framework, featuring support for multiple benchmark datasets, flexible backbone network selection, diverse vicinity selection strategies, various GAN losses and regularization penalties, exponential moving average (Karras et al. 2024), and mixed-precision training (Micikevicius et al. 2018).

For CcGAN-AVAR-S and CcGAN-AVAR-H implementations, we set N_{AV} to 50 (RC-49), 30 (RC-49-I), 400 (UTKFace), and 20 (Steering Angle). All experiments utilize a SNGAN backbone architecture with fixed hyperparameters $\lambda_{reg}^D = \lambda_{reg}^G = 1$ and $\lambda_f^G = 0.5$. The parameter λ_{dre}^D is set to 1.0 for both variants on RC-49 and for CcGAN-AVAR-H on RC-49-I, while using 0.5 in all other cases. To compute the γ -insensitive hinge loss for the regression branch of D , we pre-train a ResNet-18 model on each dataset to predict labels from images. Complete training configurations are provided in the Appendix and our codebase.

Evaluation Setup. For systematic evaluation, each trained model generates a predetermined number of images at specified evaluation centers across all datasets. On RC-49 and RC-49-I, models produce 200 fake images for each of 899 rotation angles spanning 0.1° to 89.9° in 0.1° increments. For UTKFace, models generate 1,000 images per age from 1 to 60 years. The Steering Angle evaluation employs 2,000 uniformly distributed points across $[-80^\circ, 80^\circ]$, with 50 images synthesized per point. This protocol yields total generation counts of 179,800 images (RC-49 and RC-49-I), 60,000 images (UTKFace), and 100,000 images (Steering Angle) for each evaluated method.

Following the evaluation protocol established in (Ding et al. 2023b; Ding, Wang, and Xu 2024; Ding et al. 2025), we assess generated images using one primary metric and three complementary metrics. The *Sliding Fréchet Inception Distance* (SFID) (Ding et al. 2023b) serves as our primary evaluation metric, computed as the averaged FID score across all evaluation centers. Additionally, we employ three complementary metrics: (1) the *Naturalness Image Quality Evaluator* (NIQE) (Mittal, Soundararajan, and Bovik 2012) for assessing visual realism, (2) Diversity (Ding et al. 2023b) for quantifying sample variety, and (3) Label Score (Ding et al. 2023b) for measuring label consistency. For SFID, NIQE, and Label Score, lower values indicate superior performance, whereas higher Diversity scores reflect greater sample variety. We refer interested readers to Ding et al. (2025) for complete technical details regarding these evaluation metrics.

Furthermore, we evaluate the sampling efficiency of each compared model by reporting its sampling speed (images/second) and GPU memory consumption (GiB), measured on a Linux system equipped with an NVIDIA RTX 4090D.

4.2 Experimental Results

We conduct a comprehensive evaluation of candidate methods across nine distinct settings, including eight imbalanced configurations and one balanced setting. The empirical results, presented in Tables 1 and 2 along with Figure 6, reveal

several key findings:

- The comparative analysis between RC-49 and RC-49-I reveals significant performance degradation for both vanilla CcGAN and its Dual-NDA variant when applied to the imbalanced RC-49-I dataset, demonstrating the substantial impact of data imbalance on CcGANs.
- CCDM is more robust than CcGANs with a small drop of generation performance on imbalanced datasets. However, the iterative sampling process makes CCDM 700-2000× slower at sampling than CcGAN/Dual-NDA.
- The two CcGAN-AVAR variants achieve superior performance across most settings by SFID metrics, maintaining comparable or better sample diversity than CcGAN/Dual-NDA while significantly improving label consistency - confirming the efficacy of their adaptive vicinity and auxiliary regularization designs. Crucially, CcGAN-AVAR preserves consistent generation quality between balanced (RC-49) and imbalanced (RC-49-I) datasets, unlike baseline methods that exhibit significant degradation, demonstrating exceptional robustness to data skews. Furthermore, the hybrid AV variant typically outperforms soft AV in label consistency across most configurations.
- CcGAN-AVAR achieves 300×-2000× faster generation than CCDM while maintaining sampling speeds comparable to CcGAN and Dual-NDA, along with moderate GPU memory requirements.

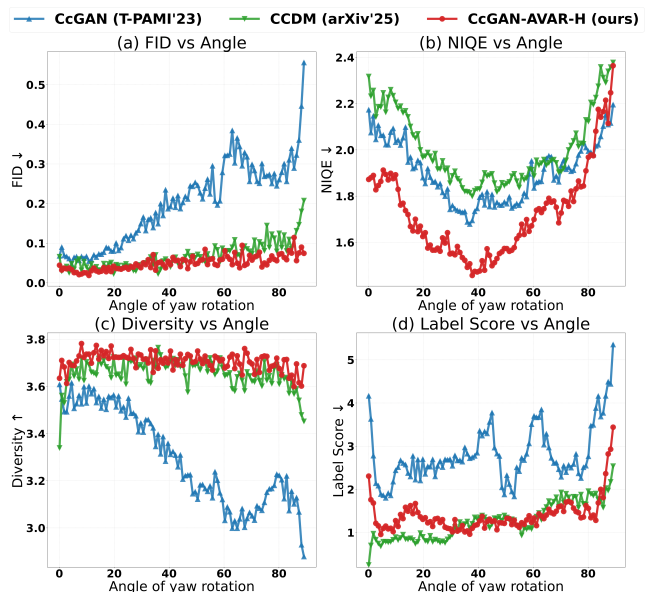


Figure 6: Visual comparison of FID, NIQE, Diversity, and Label Score versus angle (evaluation center) for three compared methods on RC-49-I (bimodal).

4.3 Ablation Study

We perform ablation studies on RC-49-I and UTKFace at 64×64 resolution to systematically evaluate the impact of individual components and CcGAN-AVAR’s key hyperparameter, as outlined below.

Dataset (resolution)	Method	SFID (primary) ↓	NIQE ↓	Diversity ↑	Label Score ↓	Speed (img/sec) ↑	Memory (GiB) ↓
RC-49 (64×64)	CcDPM (AAAI'24)	0.970	2.153	3.581	24.174	2.92	5.07
	CCDM (arXiv'25)	0.049	2.086	3.698	1.074	2.92	5.53
	CcGAN (T-PAMI'23)	0.126	1.809	3.451	2.655	6243.06	2.62
	Dual-NDA (AAAI'24)	0.148	1.808	3.344	2.211	6243.06	2.62
	CcGAN-AVAR-S	<u>0.048</u>	<u>1.728</u>	3.705	1.273	<u>4162.04</u>	<u>3.71</u>
	CcGAN-AVAR-H	<u>0.042</u>	<u>1.734</u>	3.723	<u>1.270</u>	<u>4162.04</u>	<u>3.71</u>
RC-49-I (unimodal) (64×64)	CcDPM (AAAI'24)	0.925	2.136	3.585	23.749	2.92	5.07
	CCDM (arXiv'25)	0.064	2.023	3.642	1.417	2.92	5.53
	CcGAN (T-PAMI'23)	0.151	1.880	3.400	2.487	6243.06	2.62
	Dual-NDA (AAAI'24)	0.192	1.941	3.223	2.436	6243.06	2.62
	CcGAN-AVAR-S	<u>0.054</u>	<u>1.729</u>	3.704	1.504	<u>4162.04</u>	<u>3.71</u>
	CcGAN-AVAR-H	<u>0.050</u>	<u>1.794</u>	3.711	<u>1.425</u>	<u>4162.04</u>	<u>3.71</u>
RC-49-I (bimodal) (64×64)	CcDPM (AAAI'24)	0.850	2.214	3.572	21.972	2.92	5.07
	CCDM (arXiv'25)	0.066	2.012	3.659	1.272	2.92	5.53
	CcGAN (T-PAMI'23)	0.205	1.906	3.293	2.825	6243.06	2.62
	Dual-NDA (AAAI'24)	0.235	1.886	3.162	2.317	6243.06	2.62
	CcGAN-AVAR-S	<u>0.052</u>	<u>1.736</u>	3.716	1.446	<u>4162.04</u>	<u>3.71</u>
	CcGAN-AVAR-H	<u>0.050</u>	<u>1.729</u>	<u>3.706</u>	<u>1.402</u>	<u>4162.04</u>	<u>3.71</u>
RC-49-I (trimodal) (64×64)	CcDPM (AAAI'24)	0.940	2.224	3.551	23.902	2.92	5.07
	CCDM (arXiv'25)	0.060	2.047	3.664	1.117	2.92	5.07
	CcGAN (T-PAMI'23)	0.171	1.873	3.296	2.813	6243.06	2.62
	Dual-NDA (AAAI'24)	0.168	1.949	3.302	2.575	6243.06	2.62
	CcGAN-AVAR-S	<u>0.049</u>	<u>1.735</u>	3.716	1.490	<u>4162.04</u>	<u>3.71</u>
	CcGAN-AVAR-H	<u>0.051</u>	<u>1.729</u>	<u>3.707</u>	1.462	<u>4162.04</u>	<u>3.71</u>
UTKFace (64×64)	CcDPM (AAAI'24)	0.466	<u>1.560</u>	1.211	6.868	2.10	5.70
	CCDM (arXiv'25)	0.363	1.542	1.184	6.164	2.10	6.14
	CcGAN (T-PAMI'23)	0.413	1.733	1.329	8.240	5555.56	2.44
	Dual-NDA (AAAI'24)	0.396	1.678	1.298	6.765	5555.56	2.44
	CcGAN-AVAR-S	<u>0.358</u>	1.703	<u>1.298</u>	7.222	<u>4166.67</u>	<u>3.71</u>
	CcGAN-AVAR-H	<u>0.356</u>	1.691	1.278	<u>6.696</u>	<u>4166.67</u>	<u>3.71</u>
Steering Angle (64×64)	CcDPM (AAAI'24)	0.939	<u>1.761</u>	1.150	10.999	3.33	2.28
	CCDM (arXiv'25)	0.742	1.778	1.088	5.823	3.33	2.74
	CcGAN (T-PAMI'23)	1.334	1.784	1.234	14.807	3086.42	2.50
	Dual-NDA (AAAI'24)	1.114	1.738	1.251	11.809	3086.42	2.50
	CcGAN-AVAR-S	<u>0.748</u>	1.810	1.176	<u>6.408</u>	<u>1157.41</u>	<u>3.86</u>
	CcGAN-AVAR-H	0.809	1.800	1.204	6.963	<u>1157.41</u>	<u>3.86</u>

Table 1: Comparison of generation quality and sampling efficiency at 64×64 resolution. Performance is assessed using four metrics: SFID (overall quality), NIQE (visual realism), Diversity (sample diversity), and Label Score (label consistency), along with sampling speed and GPU memory consumption measured on an RTX 4090D. “↓” (“↑”) indicates lower (higher) values are preferred. The best and second-best results are highlighted in bold and underlined, respectively.

- **The Effects of AV and Regularization:** Our component-wise analysis of CcGAN-AVAR on RC-49-I and UTKFace (Table 3) reveals that both soft and hybrid adaptive vicinity mechanisms substantially improve label consistency while maintaining or enhancing sample diversity. The auxiliary regularization terms further boost label consistency, resulting in significant overall quality improvements. It is worth noting that even the baseline configuration (without adaptive vicinity or auxiliary regularization) outperforms CcGAN/Dual-NDA (Table 1), due to a deeper GAN network and more advanced training techniques such as exponential moving average.

- **The Effects of N_{AV} :** We investigate the impact of the key hyperparameter N_{AV} on CcGAN-AVAR-H’s performance (Figure 7), conducting this ablation study with auxiliary regularization disabled to isolate AV’s effect. The results demonstrate substantial performance degradation when either disabling AV entirely ($N_{AV} = 0$) or employing an excessively wide vicinity (large N_{AV} values), while moderate N_{AV} values consistently yield acceptable results. The dashed green lines in Figure 7 correspond to the optimal values selected for our main experiments.

Dataset (resolution)	Method	SFID (primary) ↓	NIQE ↓	Diversity ↑	Label Score ↓	Speed (img/sec) ↑	Memory (GiB) ↓
UTKFace (128×128)	CcDPM (AAAI'24)	0.529	1.114	1.195	7.933	1.12	17.91
	CCDM (arXiv'25)	0.319	1.077	1.178	<u>6.359</u>	1.12	19.52
	CcGAN (T-PAMI'23)	0.367	1.113	1.199	7.747	1282.05	7.58
	Dual-NDA (AAAI'24)	0.361	<u>1.081</u>	1.257	6.310	1282.05	7.58
	CcGAN-AVAR-S	<u>0.299</u>	1.191	1.223	6.622	<u>1190.48</u>	<u>11.57</u>
	CcGAN-AVAR-H	0.297	1.173	<u>1.251</u>	6.586	<u>1190.48</u>	<u>11.57</u>
Steering Angle (128×128)	CcDPM (AAAI'24)	1.285	<u>1.989</u>	1.203	18.325	1.23	5.27
	CCDM (arXiv'25)	0.987	1.977	1.118	11.829	1.23	<u>6.85</u>
	CcGAN (T-PAMI'23)	1.689	2.411	1.088	18.438	1543.21	7.58
	Dual-NDA (AAAI'24)	1.390	2.135	<u>1.133</u>	14.099	1543.21	7.58
	CcGAN-AVAR-S	0.803	2.350	1.079	6.908	<u>1207.73</u>	11.57
	CcGAN-AVAR-H	<u>0.888</u>	2.288	1.123	<u>7.507</u>	<u>1207.73</u>	11.57
UTKFace (192×192)	CcDPM (AAAI'24)	0.970	1.522	1.187	11.224	0.80	19.93
	CCDM (arXiv'25)	0.467	1.242	1.148	7.336	0.80	22.99
	CcGAN (T-PAMI'23)	0.499	1.661	1.207	7.885	<u>617.28</u>	<u>18.18</u>
	Dual-NDA (AAAI'24)	0.487	1.483	<u>1.201</u>	6.730	<u>617.28</u>	<u>18.18</u>
	CcGAN-AVAR-S	<u>0.455</u>	1.621	1.104	<u>6.433</u>	1111.11	13.18
	CcGAN-AVAR-H	0.435	1.588	1.187	6.377	1111.11	13.18

Table 2: Comparison of generation quality and sampling efficiency at high resolutions ($> 64 \times 64$) across methods. The best and second-best results are highlighted in bold and underlined, respectively.

Dataset	Configuration				SFID (primary)	NIQE	Diversity	Label Score
	Soft AV	Hybrid AV	Aux. Reg.	Aux. DRE				
RC-49-I (bimodal) (64 × 64)	✓				0.062	1.740	3.704	2.291
	✓		✓		0.059	1.732	3.700	2.238
	✓		✓	✓	0.055	1.727	3.695	1.737
	✓		✓	✓	0.052	1.736	3.716	1.446
RC-49-I (bimodal) (64 × 64)		✓			0.062	1.740	3.704	2.291
		✓	✓		0.058	1.739	3.708	2.052
		✓	✓	✓	0.050	1.723	3.715	1.644
		✓	✓	✓	0.050	1.729	3.706	1.402
UTKFace (64 × 64)	✓				0.447	1.738	1.243	8.274
	✓		✓		0.442	1.750	1.305	7.867
	✓		✓	✓	0.432	1.747	1.307	8.073
	✓		✓	✓	0.358	1.703	1.298	7.222
UTKFace (64 × 64)		✓			0.447	1.738	1.243	8.274
		✓	✓		0.371	1.696	1.310	7.246
		✓	✓	✓	0.357	1.709	1.269	6.529
		✓	✓	✓	0.356	1.691	1.278	6.696

Table 3: Ablation study: Component-wise analysis of CcGAN-AVAR

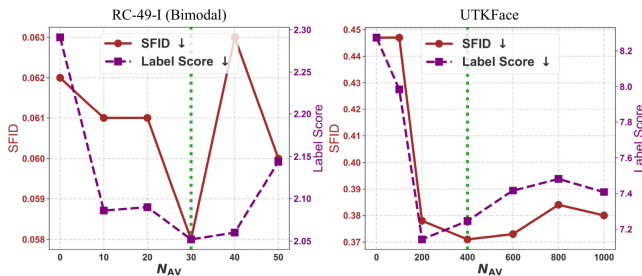


Figure 7: Ablation study: SFID/Label Score versus N_{AV}

5 Conclusion

This paper presents CcGAN-AVAR, an advanced CcGAN framework that achieves state-of-the-art generation performance while maintaining exceptional sampling efficiency. The proposed framework introduces two key innovations: (1) soft and hybrid adaptive vicinity mechanisms that effectively address the severe data imbalance inherent in regression datasets, replacing conventional fixed-size vicinity approaches; and (2) a dual regularization strategy incorporating both auxiliary regression and f -divergence penalties during generator training, significantly enhancing output quality. Ex-

tensive experiments across eight challenging imbalanced settings with varying resolutions demonstrate CcGAN-AVAR's consistent superiority over existing methods.

6 Acknowledgments

This work was supported by the National Natural Science Foundation of China (Grant No. 62306147, 62201404, U24A20326), the Natural Science Foundation of Jiangsu Province (Grant No. BK20241901), Jiangsu Supplementary Funds of National Major Talent Project (2022-2024) (Grant No. R2024PT03), Nanjing Selective Funding Initiative for Returnee Innovation Projects (Grant No. R2024LZ02), the Startup Foundation for Introducing Talent of NUIST (Grant No. 2024r056), Yangtze River Delta Community of Sci-Tech Innovation (Grant No. 2023CSJZN0301), and Pujiang Talent Program (Grant No. 23PJ1412100).

References

- Brock, A.; Donahue, J.; and Simonyan, K. 2019. Large Scale GAN Training for High Fidelity Natural Image Synthesis. In *International Conference on Learning Representations*.
- Chen, S. 2018. The Steering Angle Dataset @ONLINE. <https://github.com/SullyChen/driving-datasets>.
- Ding, X.; Wang, Y.; Wang, Z. J.; and Welch, W. J. 2023a. Efficient subsampling of realistic images from GANs conditional on a class or a continuous variable. *Neurocomputing*, 517: 188–200.
- Ding, X.; Wang, Y.; and Xu, Z. 2024. Turning Waste into Wealth: Leveraging Low-Quality Samples for Enhancing Continuous Conditional Generative Adversarial Networks. In *Proceedings of the AAAI Conference on Artificial Intelligence*, volume 38, 11802–11810.
- Ding, X.; Wang, Y.; Xu, Z.; Welch, W. J.; and Wang, Z. J. 2021. CcGAN: Continuous Conditional Generative Adversarial Networks for Image Generation. In *International Conference on Learning Representations*.
- Ding, X.; Wang, Y.; Xu, Z.; Welch, W. J.; and Wang, Z. J. 2023b. Continuous Conditional Generative Adversarial Networks: Novel Empirical Losses and Label Input Mechanisms. *IEEE Transactions on Pattern Analysis and Machine Intelligence*, 45(7): 8143–8158.
- Ding, X.; Wang, Y.; Zhang, K.; and Wang, Z. J. 2025. CCDM: Continuous conditional diffusion models for image generation. *arXiv preprint arXiv:2405.03546*.
- Fang, X.; Shen, H.-S.; and Wang, H. 2023. Diverse 3D Auxetic Unit Cell Inverse Design with Deep Learning. *Applied Physics Reviews*, 10(3).
- Ferreira, C. A.; Stepien, M.; Hosseinzadehsadati, S.; Kadeethum, T.; and Nick, H. M. 2022. Predicting the CO2 propagation in geological formations from sparsely available well data. In *16th International Conference on Greenhouse Gas Control Technologies*.
- He, K.; Zhang, X.; Ren, S.; and Sun, J. 2016. Deep Residual Learning for Image Recognition. In *Proceedings of the IEEE conference on computer vision and pattern recognition*, 770–778.
- Heyrani Nobari, A.; Chen, W.; and Ahmed, F. 2021. PcDGAN: A Continuous Conditional Diverse Generative Adversarial Network for Inverse Design. In *Proceedings of the 27th ACM SIGKDD Conference on Knowledge Discovery & Data Mining*, 606–616.
- Kang, M.; Zhu, J.-Y.; Zhang, R.; Park, J.; Shechtman, E.; Paris, S.; and Park, T. 2023. Scaling up gans for text-to-image synthesis. In *Proceedings of the IEEE/CVF conference on computer vision and pattern recognition*, 10124–10134.
- Karras, T.; Aittala, M.; Lehtinen, J.; Hellsten, J.; Aila, T.; and Laine, S. 2024. Analyzing and improving the training dynamics of diffusion models. In *Proceedings of the IEEE/CVF Conference on Computer Vision and Pattern Recognition*, 24174–24184.
- Micikevicius, P.; Narang, S.; Alben, J.; Diamos, G.; Elsen, E.; Garcia, D.; Ginsburg, B.; Houston, M.; Kuchaiev, O.; Venkatesh, G.; et al. 2018. Mixed Precision Training. In *International Conference on Learning Representations*.
- Mittal, A.; Soundararajan, R.; and Bovik, A. C. 2012. Making a “Completely Blind” Image Quality Analyzer. *IEEE Signal Processing Letters*, 20(3): 209–212.
- Miyato, T.; Kataoka, T.; Koyama, M.; and Yoshida, Y. 2018. Spectral Normalization for Generative Adversarial Networks. In *International Conference on Learning Representations*.
- Murphy, K. P. 2022. *Probabilistic machine learning: an introduction*. MIT press.
- Nowozin, S.; Cseke, B.; and Tomioka, R. 2016. f-GAN: Training generative neural samplers using variational divergence minimization. *Advances in neural information processing systems*, 29.
- Odena, A.; Olah, C.; and Shlens, J. 2017. Conditional image synthesis with auxiliary classifier gans. In *International conference on machine learning*, 2642–2651. PMLR.
- Park, T.; Kwak, J.; Ahn, H.; Lee, J.; Lim, J.; Yu, S.; Shin, C.; and Moon, T. 2022. GAN-based framework for unified estimation of process-induced random variation in FinFET. *IEEE Access*, 10: 130001–130023.
- Peebles, W.; and Xie, S. 2023. Scalable diffusion models with transformers. In *Proceedings of the IEEE/CVF International Conference on Computer Vision*, 4195–4205.
- Radford, A.; Metz, L.; and Chintala, S. 2015. Unsupervised Representation Learning with Deep Convolutional Generative Adversarial Networks. *arXiv preprint arXiv:1511.06434*.
- Triess, L. T.; Bühler, A.; Peter, D.; Flohr, F. B.; and Zöllner, M. 2022. Point Cloud Generation with Continuous Conditioning. In *International Conference on Artificial Intelligence and Statistics*, 4462–4481.
- Wu, Y.; and He, K. 2020. Group Normalization. *International Journal of Computer Vision*, 128(3): 742–755.
- Zhang, H.; Goodfellow, I.; Metaxas, D.; and Odena, A. 2019. Self-Attention Generative Adversarial Networks. In *Proceedings of the 36th International Conference on Machine Learning*, 7354–7363.
- Zhang, Z.; Song, Y.; and Qi, H. 2017. Age Progression/Regression by Conditional Adversarial Autoencoder. In *Proceedings of the IEEE Conference on Computer Vision and Pattern Recognition*, 5810–5818.

Zhao, Y.; Zhang, P.; Sun, G.; Yang, Z.; Chen, J.; and Wang, Y. 2024. CcDPM: A Continuous Conditional Diffusion Probabilistic Model for Inverse Design. In *Proceedings of the AAAI Conference on Artificial Intelligence*, volume 38, 17033–17041.

Zhu, Y.; Su, H.; Xu, P.; Xu, Y.; Wang, Y.; Dong, C.-H.; Lu, J.; Le, Z.; Yang, X.; Xuan, Q.; et al. 2023. Data augmentation using continuous conditional generative adversarial networks for regression and its application to improved spectral sensing. *Optics Express*, 31(23): 37722–37739.

Supplemental Material

A Adaptive Vicinity Implementation

A.1 Algorithm for Adaptive Vicinity Construction

Constructing the proposed soft or hybrid vicinity hinges on determining two critical parameters: the vicinity radius κ_{y_c} and the weight decay rate ν_{y_c} . A detailed procedure for computing these parameters is presented in Algorithm 1.

Algorithm 1: Soft/Hybrid Adaptive Vicinity Construction for Conditional Label y_c . Without loss of generality, we assume y_c lies between $y_{(i-1)}$ and $y_{(i)}$.

Data: Distinct training labels $Y^u = \{y_{(1)}, \dots, y_{(M)}\}$;
Sample count for each distinct training label $\{N_1, \dots, N_M\}$;

Input: Conditional label y_c ; the minimum effective sample count N_{AV} ;

Result: Vicinity width κ_{y_c} and weight decay rate ν_{y_c} .

```

1  $\kappa_l \leftarrow 0, \kappa_r \leftarrow 0$ ;
2  $N_c = 0$ ;
3  $t_l = i - 1, t_r = i$ ;
  // Vicinity extension
4 while  $N_c < N_{AV}$  do
5   if  $|y_{(t_l)} - y_c| < |y_{(t_r)} - y_c|$  then
6     // Extend leftwards
7      $\kappa_l \leftarrow |y_{(t_l)} - y_c|$ ;
8      $N_c \leftarrow N_c + N_{t_l}$ ;
9      $t_l \leftarrow t_l - 1$ ;
10  else if  $|y_{(t_l)} - y_c| > |y_{(t_r)} - y_c|$  then
11    // Extend rightwards
12     $\kappa_r \leftarrow |y_{(t_r)} - y_c|$ ;
13     $N_c \leftarrow N_c + N_{t_r}$ ;
14     $t_r \leftarrow t_r + 1$ ;
15  else
16    // Extend in both directions
17     $\kappa_l \leftarrow |y_{(t_l)} - y_c|$ ;
18     $\kappa_r \leftarrow |y_{(t_r)} - y_c|$ ;
19     $N_c \leftarrow N_c + N_{t_l} + N_{t_r}$ ;
20     $t_l \leftarrow t_l - 1$ ;
21     $t_r \leftarrow t_r + 1$ ;
22  end
23 end
24  $\kappa_{y_c} \leftarrow \max(\kappa_l, \kappa_r)$ ;
25  $\nu_{y_c} \leftarrow 1/\kappa_{y_c}$ ;

```

A.2 Heuristic Selection of N_c

The minimum number of effective samples per vicinity (N_c) serves as the crucial hyperparameter in CcGAN-AVAR, with

ablation studies on RC-49-I and UTKFace demonstrating optimal performance when N_c is properly calibrated within a moderate range, as evidenced in Figure S.8.

To determine N_c in practice, we propose a heuristic approach:

- First, identify all the distinct training labels

$$Y^u = \{y_{(1)}, \dots, y_{(M)}\} \quad (\text{S.11})$$

and their sample counts

$$\mathcal{N} = \{N_1, \dots, N_M\}. \quad (\text{S.12})$$

- Then, compute the summed counts for each and its immediate right neighbor, with results stored in

$$\mathcal{S} = \{S_1, \dots, S_{M-1}\}. \quad (\text{S.13})$$

- Finally, compute the averaged sample count $\bar{S} = \frac{1}{M-1} \sum_{i=1}^{M-1} S_i$, and set N_c to an integer near \bar{S} with potential minor adjustments based on the sparsity characteristics of the data distribution.

For instance, on the bimodal RC-49-I dataset where $\bar{S} \approx 25.279$, we set $N_c = 30$. For UTKFace with $\bar{S} \approx 480$, we chose $N_c = 400$. In the case of Steering Angle, where many $S_i \in \mathcal{S}$ cluster around 2 despite $\bar{S} \approx 13$, we selected $N_c = 20$ to mitigate the impact of sparse label regions.

B Auxiliary Regularization Implementation

B.1 Network Architecture

CcGAN-AVAR adopts a SNGAN-based architecture (Miyato et al. 2018), incorporating an additional residual block in the generator compared to the original implementation in (Ding et al. 2023b). While Ding et al. (2023b) recommends SAGAN (Zhang et al. 2019) for high-resolution scenarios, we observe that its self-attention mechanism exhibits limited compatibility with exponential moving average (EMA) (Karras et al. 2024) – a technique that effectively improves SNGAN performance in our experiments.

A key contribution of this work is our modified discriminator architecture, which integrates both a two-layer regression branch and a three-layer density ratio estimation (DRE) branch, as illustrated in Figures S.9 and S.10. The regression branch employs two linear layers with spectral normalization (SN) (Miyato et al. 2018) and ReLU activation, while the DRE branch replaces SN with group normalization (GN) (Wu and He 2020) using 8 groups. For high-resolution UTKFace (192×192) experiments, we incorporate a dropout layer after ReLU activation - crucially, not for the conventional purpose of preventing overfitting, but to address a distinct training challenge where the DRE branch otherwise fails to converge (evidenced by stagnant training loss).

Complete architectural details and implementations are provided in our code repository.

B.2 Relation to ACGAN

CcGAN-AVAR differs fundamentally from ACGAN (Odena, Olah, and Shlens 2017) in three key aspects. First, while ACGAN uses an auxiliary classification branch for class-conditional generation, its discriminator does not directly

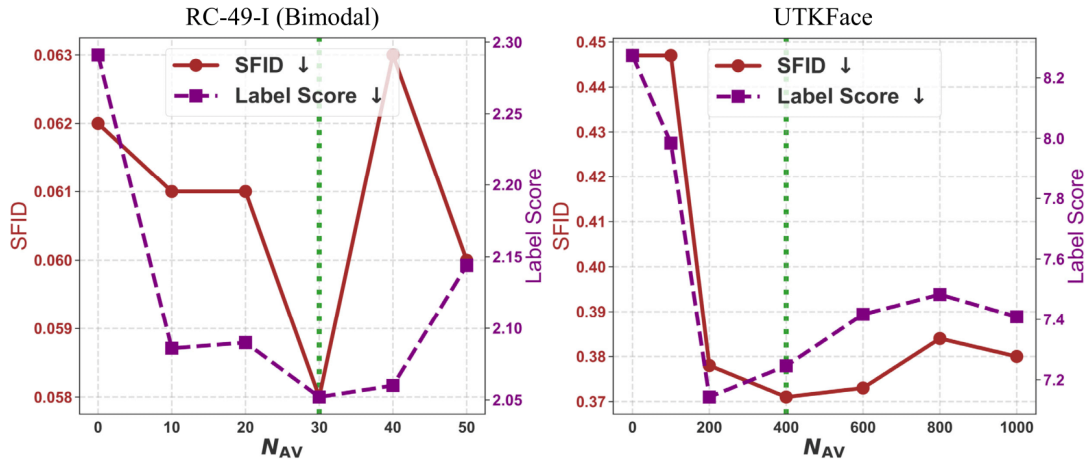


Figure S.8: Ablation analysis of adaptive vicinity size (N_c) effects on CcGAN-AVAR-H performance, comparing SFID and Label Score metrics across RC-49-I and UTKFace datasets at 64×64 resolution. Dashed green lines correspond to the parameter values used in the primary experiment. Auxiliary regularization was disabled to isolate the contribution of adaptive vicinity.

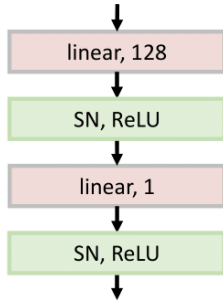


Figure S.9: Architecture of the two-layer fully connected regression branch f_{reg} in the discriminator.

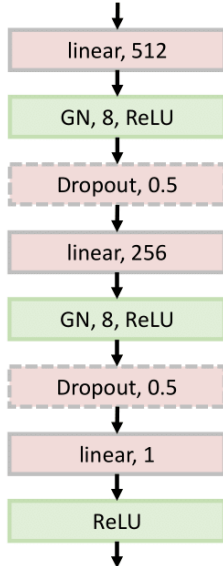


Figure S.10: Architecture of the three-layer fully connected DRE branch f_{dre} in the discriminator, where Dropout is optional.

receive class information. In contrast, CcGAN-AVAR integrates a regression branch for continuous label prediction and explicitly injects condition labels into the discriminator via label projection (Figure 3). Second, whereas ACGAN relies on a cross-entropy loss for classification, CcGAN-AVAR employs a regression loss—specifically, a custom γ -insensitive hinge loss (Eq. (6)) designed to improve robustness against label noise, rather than a standard mean squared error. Third, and most distinctively, CcGAN-AVAR implements a density ratio estimation branch that imposes an f -divergence penalty during generator training - a feature entirely absent in the standard ACGAN architecture.

B.3 Extra Illustration for f -Divergence Penalty

The f -divergence (Nowozin, Cseke, and Tomioka 2016) between $p_r(\mathbf{x}|y)$ and $p_g(\mathbf{x}|y)$ is defined as:

$$\begin{aligned} \text{Div}_f(p_r \| p_g) &= \int_{\mathcal{X}} p_g(\mathbf{x}|y) f\left(\frac{p_r(\mathbf{x}|y)}{p_g(\mathbf{x}|y)}\right) d\mathbf{x} \\ &= \mathbb{E}_{\mathbf{x} \sim p_g(\mathbf{x}|y)} \left[f\left(\frac{p_r(\mathbf{x}|y)}{p_g(\mathbf{x}|y)}\right) \right], \end{aligned} \quad (\text{S.14})$$

where f is a convex function with $f(1) = 0$. If f is a quadratic function of the form $f(t) = (t - 1)^2$, the f -divergence reduces to the Pearson χ^2 divergence:

$$\begin{aligned} \text{Div}_{\chi^2}(p_r \| p_g) &= \mathbb{E}_{\mathbf{x} \sim p_g(\mathbf{x}|y)} \left[\left(\frac{p_r(\mathbf{x}|y)}{p_g(\mathbf{x}|y)} - 1\right)^2 \right] \\ &= \mathbb{E}_{\mathbf{x} \sim p_g(\mathbf{x}|y)} [(r(\mathbf{x}|y) - 1)^2]. \end{aligned} \quad (\text{S.15})$$

The proposed f -divergence penalty of CcGAN-AVAR is defined as follows:

$$\mathcal{L}_f^G = \frac{1}{N^g} \sum_{i=1}^{N^g} (f_{\text{dre}}(D_{\text{conv}}(\mathbf{x}_i^g, y_i^g)) - 1)^2. \quad (\text{S.16})$$

In Eq. (S.16), $f_{\text{dre}}(D_{\text{conv}}(\mathbf{x}_i^g, y_i^g))$ estimates the conditional density ratio $r(\mathbf{x}|y)$. Thus, Eq. (S.16) approximates Eq. (S.15), and minimizing \mathcal{L}_f^G encourages the generator to better match the target data distribution.

C Experimental Setup and Implementation

C.1 How RC-49-I is made?

Since RC-49 is a relatively simple synthetic dataset with a sufficiently large sample size for reliable evaluation, we construct three imbalanced subsets to thoroughly assess the robustness of CcGAN-AVAR and other baseline methods. As shown in Figure S.11, these subsets exhibit unimodal, bimodal, and trimodal label distributions. Using the unimodal case as an example, we describe the derivation procedure from RC-49 as follows:

- First, we randomly select a distinct label $y_m \in Y^u$ as the mode of the imbalanced distribution.
- Second, for each element $y_{(i)}$ in Y^u excluding y_m , compute its absolute distance to y_m as $d_i = |y_{(i)} - y_m|$.
- Third, determine the mean sample count for $y_{(i)}$ using $\bar{N}_i^\circ = \max(1, \text{int}(49 \times e^{-\pi \cdot d_i}))$, where π is a decay rate (set to 0.1 for unimodal distributions). The final sample count for $y_{(i)}$ is then calculate with noise perturbation: $N_i^\circ = \min(49, \max(0, \text{int}(\bar{N}_i^\circ + \mathcal{N}(0, 5))))$
- Finally, we construct RC-49-I (unimodal) in a label-by-label manner by randomly selecting N_i° images from the complete set of 49 images for each $y_{(i)}$.

The bimodal and trimodal subsets require a more sophisticated generation procedure, with full implementation details available in our codebase.

C.2 Hardware and Software Details

All experiments were conducted on NVIDIA RTX 4090D servers with the following hardware configurations:

- 64×64 resolution: 24GB GPU memory
- 128×128 and 192×192 resolutions: 48GB GPU memory (RTX 4090D-48G)

The key software requirements include:

- **Operating System:** Ubuntu 22.04 LTS
- **GPU Computing:** CUDA 12.8
- **Core Software:** Python 3.12.7; MATLAB R2021b
- **Python Packages:** torch 2.7.0; torchvision 0.22.0; accelerate 1.6.0; numpy 1.26.4; scipy 1.13.1; h5py 3.11.0; Pillow 10.4.0; matplotlib 3.9.2

C.3 Training Configuration Details

For CcGAN-AVAR implementation, we train a ResNet-18 model from scratch on each dataset’s training set to predict image regression labels, using 200 epochs with a batch size of 256, base learning rate of 0.01, weight decay of 10^{-4} , and enabled mixed-precision training.

Table S.4 details our CcGAN-AVAR training configurations, which employ a modified SNGAN backbone with exponential moving average and mixed-precision training - improvements over Ding et al. (2023b)¹ and Ding, Wang, and Xu (2024)². Through mixed-precision training, our implementation demonstrates a 2× improvement in training speed

and 50% reduction in memory usage compared to Ding et al. (2023b) when using identical architecture and batch size configurations.

C.4 Evaluation Configuration Details

Our evaluation protocol follows Ding et al. (2023b); Ding, Wang, and Xu (2024); Ding et al. (2025), with detailed specifications provided in Appendix S.V.B of Ding et al. (2025). For the RC-49-I experiments, we maintain identical evaluation procedures to those used for RC-49.

D Extra Experimental Results

Example synthetic images generated by Dual-NDA and CcGAN-AVAR for the UTKFace and Steering Angle experiments (128×128 resolution) are presented in Figs. S.12 and S.13.

¹https://github.com/UBCDingXin/improved_CcGAN

²<https://github.com/UBCDingXin/Dual-NDA>

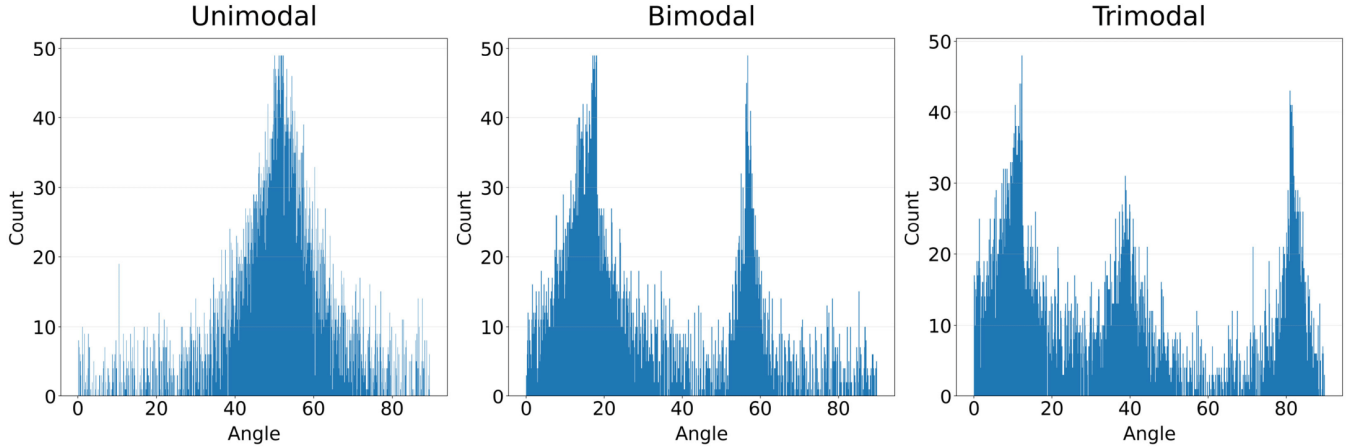


Figure S.11: Three data imbalance patterns in RC-49-I

Dataset	Configuration
RC-49	SNGAN, gene_ch=64, disc_ch=48, hinge loss, DiffAugment, use EMA, steps=50K, batch size=256, lr=10 ⁻⁴ , num_D_steps=2, N _{AV} = 50, λ _{dre} = 10 ⁻² , λ _{reg} ^D = λ _{reg} ^G = 1, λ _{dre} ^G = 1, λ _f ^G = 0.5
RC-49-I (unimodal)	SNGAN, gene_ch=64, disc_ch=48, hinge loss, DiffAugment, use EMA, steps=50K, batch size=256, lr=10 ⁻⁴ , num_D_steps=2, N _{AV} = 50, λ _{dre} = 10 ⁻² , λ _{reg} ^D = λ _{reg} ^G = 1, λ _{dre} ^G = 1 (hybrid), λ _{dre} ^G = 0.5 (Soft), λ _f ^G = 0.5
RC-49-I (bimodal)	SNGAN, gene_ch=64, disc_ch=48, hinge loss, DiffAugment, use EMA, steps=50K, batch size=256, lr=10 ⁻⁴ , num_D_steps=2, N _{AV} = 50, λ _{dre} = 10 ⁻² , λ _{reg} ^D = λ _{reg} ^G = 1, λ _{dre} ^G = 1 (hybrid), λ _{dre} ^G = 0.5 (Soft), λ _f ^G = 0.5
RC-49-I (trimodal)	SNGAN, gene_ch=64, disc_ch=48, hinge loss, DiffAugment, use EMA, steps=50K, batch size=256, lr=10 ⁻⁴ , num_D_steps=2, N _{AV} = 50, λ _{dre} = 10 ⁻² , λ _{reg} ^D = λ _{reg} ^G = 1, λ _{dre} ^G = 1 (hybrid), λ _{dre} ^G = 0.5 (Soft), λ _f ^G = 0.5
UTKFace (64×64)	SNGAN, gene_ch=64, disc_ch=48, hinge loss, DiffAugment, use EMA, steps=50K, batch size=256, lr=10 ⁻⁴ , num_D_steps=2, N _{AV} = 400, λ _{dre} = 10 ⁻² , λ _{reg} ^D = λ _{reg} ^G = 1, λ _{dre} ^G = 0.5, λ _f ^G = 0.5
Steering Angle (64×64)	SNGAN, gene_ch=64, disc_ch=64, hinge loss, DiffAugment, use EMA, steps=200K (hybrid) / 190K (soft), batch size=256, lr=10 ⁻⁴ , num_D_steps=1, N _{AV} = 20, λ _{dre} = 10 ⁻² , λ _{reg} ^D = λ _{reg} ^G = 1, λ _{dre} ^G = 0.5, λ _f ^G = 0.5
UTKFace (128×128)	SNGAN, gene_ch=64, disc_ch=48, hinge loss, DiffAugment, use EMA, steps=60K, batch size=128, lr=10 ⁻⁴ , num_D_steps=2, N _{AV} = 400, λ _{dre} = 10 ⁻² , λ _{reg} ^D = λ _{reg} ^G = 1, λ _{dre} ^G = 0.5, λ _f ^G = 0.5
Steering Angle (128×128)	SNGAN, gene_ch=64, disc_ch=48, hinge loss, DiffAugment, use EMA, steps=200K (hybrid) / 190K (soft), batch size=128, lr=10 ⁻⁴ , num_D_steps=1, N _{AV} = 20, λ _{dre} = 10 ⁻² , λ _{reg} ^D = λ _{reg} ^G = 1, λ _{dre} ^G = 0.5, λ _f ^G = 0.5
UTKFace (192×192)	SNGAN, gene_ch=64, disc_ch=48, hinge loss, DiffAugment, use EMA, steps=70K (hybrid) / 50K (soft), batch size=128, lr=10 ⁻⁴ , num_D_steps=2, N _{AV} = 400, λ _{dre} = 10 ⁻² , λ _{reg} ^D = λ _{reg} ^G = 1, λ _{dre} ^G = 0.5, λ _f ^G = 0.5, DRE branch uses Dropout

Table S.4: Training Configurations for CcGAN-AVAR

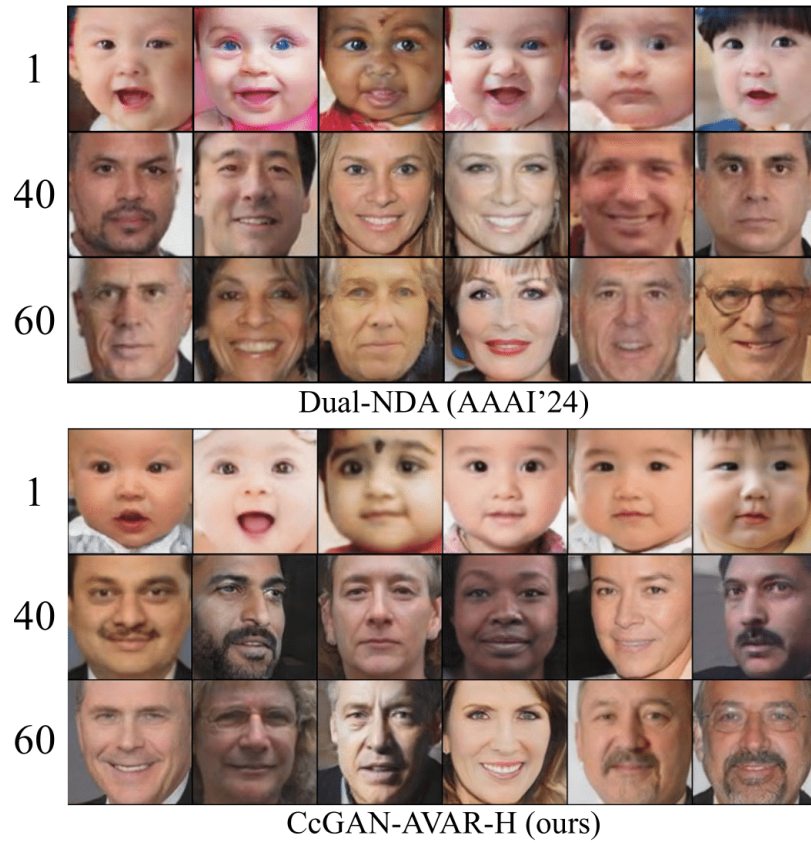


Figure S.12: Some example fake images from Dual-NDA and CcGAN-AVAR-H in the UTKFace (128×128) experiment.

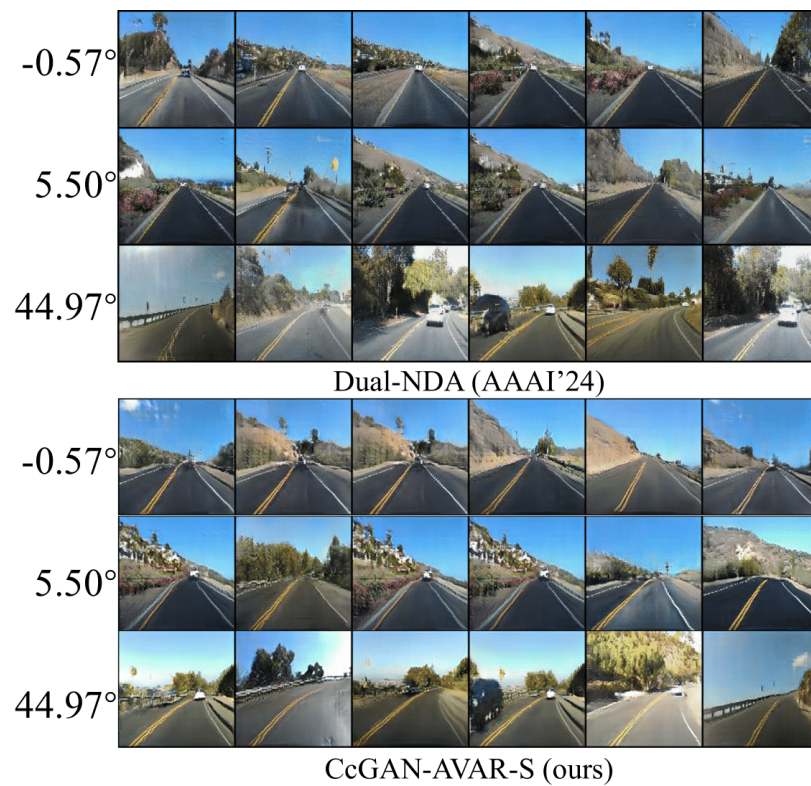


Figure S.13: Some example fake images from Dual-NDA and CcGAN-AVAR-H in the Steering Angle (128×128) experiment.